Available online at www.sciencedirect.com
SCIENCE DIRECT®
Journal of Sound and Vibration 280 (2005) 379–400
JOURNAL OF SOUND AND VIBRATION
www.elsevier.com/locate/jsvi

# Controllability assessment of plate-like structures with uncertainties under piezoelectric actuation

Y.Y. Li[1], L. Cheng*

*Department of Mechanical Engineering, The Hong Kong Polytechnic University, Hung Hom, Kowloon, Hong Kong SAR, China*

Received 14 November 2002; accepted 12 December 2003

**Abstract**

A controllability assessment of plate-like structures with uncertainties under piezoelectric actuation is performed in this paper. Different from the previous studies, a novel index is proposed to quantify the degree of controllability using the sensor/actuator transfer function. Influences of unmodelled high-frequency dynamics and structural parameter variations on controllability are discussed, and the relationship between the indices for the nominal and uncertain cases is derived. In order to validate the controllability assessment numerically, the modelling of a plate with piezoelectric actuation is developed with the consideration of the full coupling between the PZT actuators and the host plate, and verified by experiments. It is demonstrated that a proper design of the polyvinylidene flouride sensor would help eliminate effects of higher order modes on the basis of strain mode shapes. Since the latter is very sensitive to the mass and stiffness added by PZT actuators, the dynamics of PZT actuators must be taken into account during the design, as opposed to the case where a point transducer is used.


## 1. Introduction

Plate-like structures with active device are important components which are extensively used in mechanical, aeronautical and structural engineering, in which piezoelectric materials are frequently used as actuators and/or sensors due to their intrinsic direct and converse piezoelectric effects. For years, vibration control of this type of structures has been a major research topic, and led to the development of various control strategies [1–5].

*Corresponding author. Tel.: +852-2766-6769; fax: +852-2365-4703.
*E-mail address:* mmlcheng@polyu.edu.hk (L. Cheng).
[1] On leave from Department of Mechanical Engineering, Fuzhou University, Fujian 350001, China.

0022-460X/$ - see front matter © 2003 Elsevier Ltd. All rights reserved.
doi:10.1016/j.jsv.2003.12.015

During the controller design process, one of the important issues to be considered is the controllability analysis. A high degree of controllability allows one to obtain a better performance with the least number of actuators and minimum control effort. This issue has received much attention from both qualitative (whether a system is controllable) [6,7] and quantitative (to what extent a system is controllable) point of view [8–10].

In general, the quantitative analysis of controllability not only provides information on selecting the most dominant modes for control, but also assesses the degree of controllability. A popular way is to define the controllability indices by measuring the degree of controllability of each mode [11] or to use the minimum singular value of the controllability Gramian [10,12]. These indices have shown great merits in many cases. However, for the structure with uncertainties, which can be caused by parameter variations, higher order mode truncation, etc., it is difficult to measure the degree of each mode or to solve the Gramian determinately. In such cases, the previous indices cannot reflect the variation tendency of controllability accurately.

As is known, the controllability relates to the selection of actuator locations, which leads to very different frequency response function (FRF) $H(\omega)$ and accordingly affects the design of controllers, especially in the design of $H^{\infty}$ or $\mu$-controllers. This paper presents an attempt to develop an index based on the FRF for controllability assessment in the case of structures with uncertainties. It is pertinent to mention that this study does not emphasize either on the theoretical derivation of the sufficient and necessary conditions, which is always done for the robust controllability analysis, or on the controller design. It will rather provide a feasible way to assess the controllability of a given system and further illustrate changes of degree of controllability due to the parameter variations and higher order modes.

The paper is organized in four sections including the Introduction. In Section 2, the modelling of a plate with piezoelectric patches is performed and validated by experiments. In Section 3, an index is defined to measure the degree of controllability. Influences of unmodelled high-frequency dynamics and parameter variations on controllability index are examined. Numerical results on the effect of PZTs on strain nodal lines, the elimination of high order modes using PVDF sensors, and the variation tendency of controllability index under parameter changes are discussed. Finally, some conclusions are drawn.

## 2. Modelling of a plate with piezoelectric actuation

In order to formulate the transfer functions between the PZTs (as actuators) and polyvinylidene fluoride (PVDFs) (as sensors), the modelling of a plate with piezoelectric actuation is developed, in which the equation of motion is cast in a state-space form so as to obtain a set of FRFs.

Consider a rectangular plate ($2a \times 2b \times 2h$) with $r$ pairs of piezoelectric patches $\Omega_{pe_k}$: $\{x_{pe_{k1}} \leqslant x \leqslant x_{pe_{k2}}, y_{pe_{k1}} \leqslant y \leqslant y_{pe_{k2}},\ k = 1, \ldots, r\}$ on both sides of the structure as shown in Fig. 1. It is assumed that perfect bonding between the plate and the piezoelectric elements with zero glue thickness is realized so as to ensure the continuity of deflection at all interfaces. According to the first order shear deformation plate theory, the stress–strain relations without considering the transverse shear stresses can be expressed as [13,14]

$$\{\sigma\} = [S]\{\varepsilon - \upsilon\}, \tag{1}$$

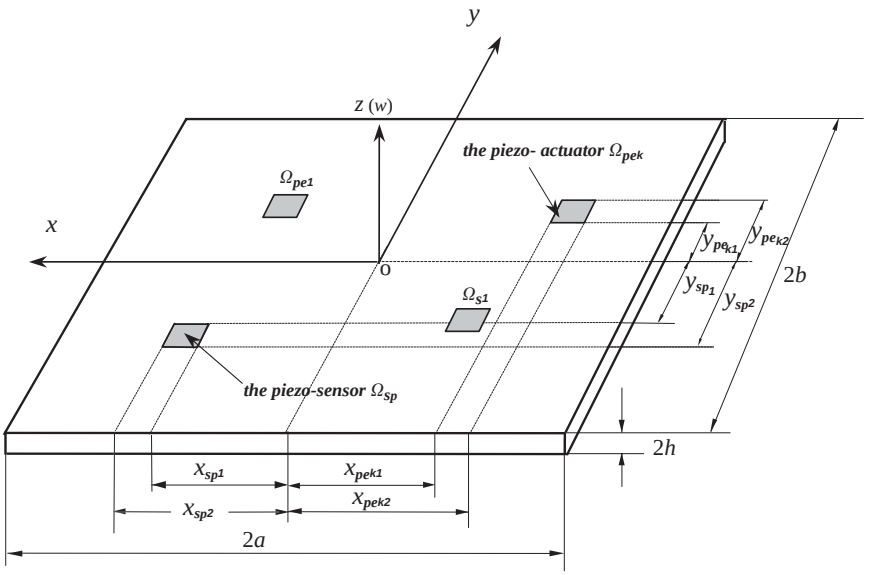


Fig. 1. Schematic diagram of a plate with piezoelectric actuation.

where $\{\sigma\} = \{\sigma_x \ \sigma_y \ \sigma_{xy}\}^{\mathrm{T}}$ is the stress vector and $\{\varepsilon\}$ the strain vector. $S$ is the elastic stiffness matrix satisfying

$$[S]_{pl} = \frac{E_{pl}}{1 - v_{pl}^2} \begin{bmatrix} 1 & v_{pl} & 0 \\ v_{pl} & 1 & 0 \\ 0 & 0 & \dfrac{(1 - v_{pl})}{2} \end{bmatrix} \tag{2a}$$

for the plate and

$$[S]_{pe} = \frac{E_{pe}}{1 - v_{pe}^2} \begin{bmatrix} 1 & v_{pe} & 0 \\ v_{pe} & 1 & 0 \\ 0 & 0 & \dfrac{(1 - v_{pe})}{2} \end{bmatrix} \tag{2b}$$

for the piezoelectric patch

$$\{\upsilon\} = \frac{V_k d}{h_{pe}} \begin{Bmatrix} 1 \\ 1 \\ 0 \end{Bmatrix} \chi_{pe_k}(x, y), \quad k = 1, \ldots, r. \tag{3}$$

$(E_{pl}, v_{pl})$ and $(E_{pe}, v_{pe})$ are the Young's modulus and Poisson ratio of the plate and piezoelectric patch, respectively. $h_{pe}$, $V_k$ and $d$ are the thickness of the piezoelectric patch, the input voltage applied on the $k$th actuator patches and the piezoelectric strain coefficients, respectively. $\chi_{pe_k}(x, y)$

is the generalized location function described by the Heaviside function H as [14,15]

$$\chi_{pe_k}(x,y) = [\mathrm{H}(x - x_{pe_{k1}}) - \mathrm{H}(x - x_{pe_{k2}})][\mathrm{H}(y - y_{pe_{k1}}) - \mathrm{H}(y - y_{pe_{k2}})]. \tag{4}$$

In the light of the stress resultants

$$\begin{Bmatrix} M_x \\ M_y \\ M_{xy} \end{Bmatrix} = \int \begin{Bmatrix} \sigma_x \\ \sigma_y \\ \sigma_{xy} \end{Bmatrix} z \, \mathrm{d}z, \tag{5}$$

the moments under the presence of piezoelectric patch are determined as

$$\begin{aligned} M_x &= \frac{E_{pl}h^3}{12(1-v_{pl}^2)}(\kappa_x + v_{pl}\kappa_y) + \sum_{k=1}^{r} \frac{E_{pe}}{1-v_{pe}}\left[\frac{2l_1(\kappa_x + v_{pe}\kappa_y)}{3(1+v_{pe})} - \frac{l_2}{h_{pe}} V_k d\right]\chi_{pe_k}(x,y), \\ M_y &= \frac{E_{pl}h^3}{12(1-v_{pl}^2)}(\kappa_y + v_{pl}\kappa_x) + \sum_{k=1}^{r} \frac{E_{pe}}{1-v_{pe}}\left[\frac{2l_1(\kappa_y + v_{pe}\kappa_x)}{3(1+v_{pe})} - \frac{l_2}{h_{pe}} V_k d\right]\chi_{pe_k}(x,y), \\ M_{xy} &= \kappa_{xy}\left[\frac{E_{pl}h^3}{24(1+v_{pl})} + \sum_{k=1}^{r} \frac{E_{pe}l_1}{3(1+v_{pe})}\chi_{pe_k}(x,y)\right], \end{aligned} \tag{6}$$

where $\kappa_x = -\partial^2 w/\partial x^2$, $\kappa_y = -\partial^2 w/\partial y^2$, $\kappa_{xy} = -2\partial^2 w/\partial x \partial y$. $w$ denotes the mid-plane transverse displacement of point $(x,y)$ either on the plate or on the piezoelectric element. $l_1$ and $l_2$ are two coefficients defined as [15]

$$l_1 = (h + h_{pe})^3 - h^3, \qquad l_2 = (h + h_{pe})^2 - h^2. \tag{7}$$

In general, the equilibrium equation of the plate induced by the applied electric field is given by

$$\frac{\partial^2 M_x}{\partial x^2} + 2\frac{\partial^2 M_{xy}}{\partial x \partial y} + \frac{\partial^2 M_y}{\partial y^2} = \rho h \frac{\partial^2 w}{\partial t^2}, \tag{8}$$

where $\rho$ is the mass per unit volume combining the material properties of plate ($\rho_{pl}$) and piezoelectric patch ($\rho_{pe}$). Substituting Eq. (6) into (8) and denoting the equivalent flexural rigidity $D_0$ as

$$D_0 = \left[\frac{E_{pl}h^3}{12(1-v_{pl}^2)} + \sum_{k=1}^{r} \frac{2E_{pe}l_1}{3(1-v_{pe}^2)}\chi_{pe_k}\right], \tag{9}$$

one has

$$D_0 \nabla^4 w + \rho h \frac{\partial^2 w}{\partial t^2} = \sum_{k=1}^{r} D_k V_k, \tag{10}$$

where

$$\begin{aligned} \nabla^2 &= (\partial^2/\partial x^2 + \partial^2/\partial y^2), \\ D_k &= -\frac{E_{pe}l_2 d}{h_{pe}(1-v_{pe})}\left(\frac{\partial^2 \chi_{pe_k}(x,y)}{\partial x^2} + \frac{\partial^2 \chi_{pe_k}(x,y)}{\partial y^2}\right). \end{aligned} \tag{11}$$

Eq. (10) describes the displacement equation of motion of the plate with piezoelectric actuation in a formal way. The effect of piezoelectric patches on deflection is included through the rigidity

coefficients $(D_0, D_k)$, the combined mass density $\rho$ and the input voltage $V_k$. Eq. (11) shows the physical effect of the PZT as a distributed line moment applied along the edges [14]. In practice, however, Eq. (10) is difficult to handle. Consequently, a parallel variational approach is developed to calculate the mode shape functions of the plates with PZT patches $\phi_{ij}(x, y)$ detailed later.

The transverse displacement $w(x, y, t)$ can expressed as a superposition of modes as

$$w(x, y, t) = \sum_{i=1}^{\infty} \sum_{j=1}^{\infty} \phi_{ij}(x, y)\eta_{ij}(t). \tag{12}$$

Eq. (10) with the consideration of structural damping and mode truncation denoted by the nominal system can therefore be rewritten by a set of differential equations as

$$\ddot{\eta}_{ij}(t) + 2\zeta_{ij}\omega_{ij}\dot{\eta}_{ij}(t) + \omega_{ij}^2\eta_{ij}(t) = \sum_{k=1}^{r} \frac{V_k}{\rho hab} \int\int_{\Omega_{pe_k}} D_k\phi_{ij}(x, y)\,\mathrm{d}x\,\mathrm{d}y \quad (i = 1, \ldots, m,\ j = 1, \ldots, n), \tag{13}$$

where $\eta_{ij}(t)$, $\phi_{ij}(x, y)$, $\omega_{ij}$ and $\zeta_{ij}$ are the $ij$th modal co-ordinate, shape function, natural frequency and damping ratio, respectively. $(m, n)$ are the numbers of modes after the truncation. Using the transformation $Q(t) = \{\dot{\eta}(t)^{\mathrm{T}}\ \eta(t)^{\mathrm{T}}\}^{\mathrm{T}}$, Eq. (13) is re-expressed in the state-space form as

$$\dot{Q}(t) = \mathbf{A}Q(t) + \mathbf{B}U(t), \tag{14}$$

where

$$U(t) = \begin{Bmatrix} V_1 \\ \vdots \\ V_r \end{Bmatrix}_{r\times 1}, \quad \mathbf{A} = \begin{bmatrix} \mathbf{0} & \mathbf{I} \\ [-\omega_{ij}^2] & [-2\zeta_{ij}\omega_{ij}] \end{bmatrix}_{2mn\times 2mn},$$

$$\mathbf{B} = \begin{bmatrix} [\mathbf{0}] \\ \cdots \\ \cdots b_{ij}(x_{pe_k}, y_{pe_k}) \cdots \\ \cdots \end{bmatrix}_{2mn\times r},$$

$$b_{ij}(x_{pe_k}, y_{pe_k}) = \frac{1}{\rho hab} \int\int_{\Omega_{pe_k}} D_k\phi_{ij}(x, y)\,\mathrm{d}x\,\mathrm{d}y. \tag{15}$$

In general, matrices $(\mathbf{A},\mathbf{B})$ and the left eigenvectors are taken to analyze the degree of controllability using the controllability Gramian [11] or modal controllability theory [6]. For example, $\mathbf{A}$ and $\mathbf{B}$ are essential to the solution of controllability Gramian matrix $\mathbf{W}_c$ from the Lyapunov equation

$$\mathbf{A}\mathbf{W}_c + \mathbf{W}_c\mathbf{A}^{\mathrm{T}} + \mathbf{B}\mathbf{B}^{\mathrm{T}} = \mathbf{0}, \tag{16}$$

in which the controllability is assessed from the singular values of $\mathbf{W}_c$. However, for a complicated structure, the inevitable error of structural parameter identification, e.g., $\omega_{ij}$ and $\zeta_{ij}$, results in a variation of $\mathbf{A}$, which makes it difficult to analyze the controllability from Eq. (16) determinately. In addition, the spillover caused by the truncation of high-frequency modes might shift the poles of closed-loop system to the unstable region and also evoke some uncontrollable modes. In order

to investigate these influences on the controllability, Eq. (14) with the consideration of high-frequency modes and parameter variations denoted by the uncertain system is rewritten as

$$\dot{Q}(t) = \mathbf{A}_u Q(t) + \mathbf{B}_u U(t), \tag{17}$$

where

$$\mathbf{A}_u = \begin{bmatrix} \mathbf{0} & \mathbf{I} \\ [-\tilde{\omega}_{ij}^2] & [-2\tilde{\zeta}_{ij}\tilde{\omega}_{ij}] \end{bmatrix}, \quad \mathbf{B}_u = \begin{bmatrix} [\mathbf{0}] \\ \begin{bmatrix} \cdots \\ \cdots b_{ij}(x_{pe_k}, y_{pe_k}) \cdots \\ \cdots \end{bmatrix} \end{bmatrix}. \tag{18}$$

The symbol '$\sim$' over $\omega_{ij}$ and $\zeta_{ij}$ represents the actual quantity of natural frequencies and damping ratios obtained from system identification. Eq. (17) describes the dynamics of the plate under PZT actuation. Since the controllability assessment discussed later is based on the transfer function, which relates the sensor output to actuator input, the sensor output equation is required. In general, accelerometers, strain gauges or PVDF film can be used as the sensors. Thanks to its direct effect, PVDF film made of piezoelectric material produces electric charges once deformed. Bonded on the surface of the plate, the charge produced is proportional to the strain over the area it covers. For a subset of charge signals measured by $p$ PVDF sensors, the charge output $\mathbf{y}(t)$ is given by

$$\mathbf{y}(t) = \mathbf{C}_u Q(t), \tag{19}$$

where

$$\mathbf{C}_u = \begin{bmatrix} \begin{bmatrix} \cdots \\ \cdots c_{ij}(x_{s_l}, y_{s_l}) \cdots \\ \cdots \end{bmatrix} & [\mathbf{0}] \end{bmatrix}, \tag{20a}$$

$$c_{ij}(x_{s_l}, y_{s_l}) = -\frac{(h + h_{pvdf})}{2} \int\int_{\Omega_{s_l}} \left( e_{31} \frac{\partial^2 \phi_{ij}}{\partial x^2} + e_{32} \frac{\partial^2 \phi_{ij}}{\partial y^2} \right) \mathrm{d}x\, \mathrm{d}y, \quad l = 1, \ldots, p, \tag{20b}$$

in which $h_{pvdf}$ is the thickness of the PVDF, $e_{31}$ and $e_{32}$ are the piezoelectric stress constants, and $e_{31} = e_{32}$ if there is no skew angle or the PVDF sensor is equally poled. Knowing the capacitance of the sensor, the charge signal can be converted to a voltage signal using charge amplifiers.

Clearly, the FRF from the $k$th piezoelectric actuation to the $l$th PVDF response for the uncertain system can be expressed by $\tilde{H}_{kl}(\omega)$ as

$$\tilde{H}_{kl}(\omega) = \frac{y_l(\omega)}{U_k(\omega)} = \sum_{i=1}^{\infty} \sum_{j=1}^{\infty} \frac{c_{ij}(x_{si}, y_{si}) b_{ij}(x_{pe_k}, y_{pe_k})}{(\tilde{\omega}_{ij}^2 - \omega^2) + 2j\tilde{\zeta}_{ij}\tilde{\omega}_{ij}\omega}, \quad k = 1, \ldots, r, \;\; l = 1, \ldots, p. \tag{21}$$

Eq. (21) shows that $\tilde{H}_{kl}(\omega)$ obtained from the FRF comprise information about actuator locations, which is related to the analysis of controllability. The problem hereafter is to find a feasible index, and then to explore the controllability in the cases of high-frequency mode truncation, structural parameter variations, etc.

The above procedures describe the derivation of the transfer function used for controllability analysis. In most cases, however, structural mode shapes with patched PZT actuators can hardly

be known analytically. For this reason, a parallel formulation based on the variational principle is developed to obtain the mode shape function or to calculate the response of the system under PZT actuation. In summary, a set of uniformly distributed springs, working in both translation and rotation, is used along the four edges of the plate. A proper assignment of the spring stiffness would allow simulation of different boundary conditions. The Hamiltonian of the system, including both kinetic energy and potential energy of the plate, PZT actuators, boundary springs and enthalpy density can be formulated. Using a polynomial decomposition in both $x$ and $y$ directions and applying Lagrange equation yields a set of linear differential equations. These equations can then be resolved to find the natural frequencies and mode shapes of the system. As a result, the aforementioned procedure can then be applied. As an alternative, the whole set of equations can be directly resolved to compute structural response under PZT actuation. Readers are referred to Ref. [16] for more details.

The validity of the modelling is verified by comparing numerical simulations to experimental tests using a free aluminum plate. The plate contains a pair of PZT patches (Sensortech BM500), which were bonded on the two opposite sides of the plate at location $\Omega_{pe}$: $[-0.055 - 0.005] \times [0.007\ 0.057]$ m$^2$. Dimensions and material properties of the plate and the PZTs are tabulated in Table 1. For the numerical modelling, a software package using *Matlab* was developed, in which Newmark method was adopted to solve the state-space equation so as to obtain the FRF [17]. For experiment, pseudo-random signal was generated by a TGA 1230 signal generator, then amplified by a Trek Piezo-Driver (Model 607), and exerted on the PZT pair. The responses of the plate were measured using B&K 4397 accelerometers and analyzed by the B&K 3023 signal analyzer [18]. Fig. 2 shows the FRF curves at location $(-0.106, 0.095)$, which are obtained from the numerical simulation and experimental test, respectively. It can be observed that apart from the very-low-frequency region containing experimental noise, tendencies of the two FRF curves are basically the same. Before 350 Hz, resonant peaks of these two curves coincide with each other. At higher-frequency region, a slight shift between the two curves occurs. It is appropriate to mention that calculations used nominal values for different parameters related to material properties. No attempt was made to match simulations with experiments by adjusting these parameters. One plausible explanation for this shift is that perfect bonding between the host structure and PZTs was assumed in the model, while in reality the connection between both was less rigid. Therefore, the model seems to overestimate the stiffness of the system, which apparently becomes more obvious in the high-frequency region. As a whole, however, the model gives very satisfactory results.

Table 1
Components characteristics

| Material | Plate (aluminium) | Actuator (piezoceramic) | Sensor (PVDF) |
|---|---|---|---|
| Dimension (m) | $0.34 \times 0.24$ | $0.05 \times 0.05$ | $0.008 \times 0.012$ |
| Thickness (m) | 2E–03 | 5E–04 | 5.2E–05 |
| Mass density (kg/m$^3$) | 2700 | 7650 | 1780 |
| Young's modulus (GPa) | 71 | 64.5 | 3 |
| Poisson ratio | 0.3 | 0.3 | — |
| Piezo. constant ($e_{31}$) (N/mV) | — | 10.32 | 0.217 |
| Loss factor | 0.01 | — | — |

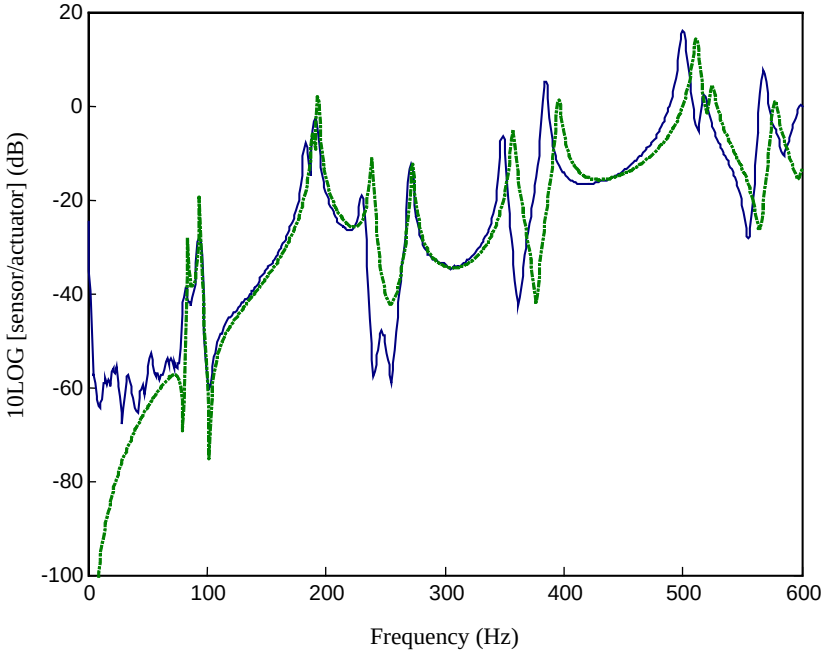


Fig. 2. The FRF with PZT at $\Omega_{pe}$ and accelerometer at $(-0.106, 0.095)$ (unit: m). — Experimental result; - - - numerical result.

## 3. Controllability assessment

### 3.1. Controllability index

Without loss of generality, the transfer function from the $k$th piezoelectric actuator to the $l$th PVDF response is described as

$$H_{kl}(\omega) = \sum_{i=1}^{m} \sum_{j=1}^{n} \frac{c_{ij}(x_{s_l}, y_{s_l}) b_{ij}(x_{pe_k}, y_{pe_k})}{[(\omega_{ij}^2 - \omega^2) + 2j\zeta_{ij}\omega_{ij}\omega]}. \tag{22}$$

Clearly, $H_{kl}(\omega)$ depends on the natural frequency, $b_{ij}(x_{pe_k}, y_{pe_k})$ and $c_{ij}(x_{s_l}, y_{s_l})$, in which the latter two are crucial for the determination of balanced controllability and observability Gramians. As is known, the Hankel singular value of Gramian reflects the degree of controllability, in which a high value indicates a more controllable mode. That is to say, the modal Hankel singular value can measure balanced controllability and observability of each resonance mode to deselect insignificant resonance modes [19]. On the other hand, there exists a relationship between the $kl$th Hankel singular value and the norm of transfer function $H_{kl}(\omega)$, i.e., $\|H_{kl}(\omega)\|$ at the resonant frequency [20,21]. It is therefore possible to develop an index based on $H_{kl}(\omega)$ for controllability assessment. An intuitive observation is that when the locations of actuators are ascertained, the controllability of the system will be consequently determined. In

terms of $H_{kl}(\omega)$, a certain $ij$th mode is controllable when the coefficient $b_{ij} \neq 0$, whereas when $b_{ij} = 0$, the $ij$th mode will be uncontrollable.

An ideal controllability index should reflect the degree of controllability subject to unmodelled dynamics and structural parameter variations. Considering the fact that the unmodelled dynamics (e.g., the effect of high-frequency modes) can be included in the $\|H_{kl}(\omega)\|$ (described later in Eq. (24)), and parameter variations (mass, stiffness or damping) affect the natural frequency and damping ratio, which can be embodied in the resonance bandwidth $D_{ij} = 2\zeta_{ij}\omega_{ij}$, an index $\beta_{ij}$ involving the average resonance amplitude at frequency $\omega = \omega_{ij}$ and the resonance bandwidth is defined as

$$\beta_{ij} = \frac{1}{rp} \sum_{k=1}^{r} \sum_{l=1}^{p} \|H_{kl}(\omega_{ij})\| \sqrt{D_{ij}}, \quad D_{ij} = 2\zeta_{ij}\omega_{ij}, \quad i = 1, \ldots, m, \; j = 1, \ldots, n, \tag{23}$$

where $\|H_{kl}(\omega_{ij})\|$ is the norm $H_{kl}$ at frequency $\omega = \omega_{ij}$ (see Fig. 3). When the PZT is placed at the largest deformation region of the mode $ij$, $b_{ij}$ achieves its maximum, leading to a high value of $\|H_{kl}(\omega_{ij})\|$ and $\beta_{ij}$.

### 3.2. Controllability assessment

The effects of unmodelled high-frequency dynamics ($i \geqslant m+1$, $j \geqslant n+1$) and parameter variations on controllability index are analyzed. To gain further insights into the relationship between $\tilde{H}_{kl}(\omega)$ for the uncertain system and $H_{kl}(\omega)$ for the nominal system, Eq. (21) is re-organized in three parts as follows:

$$\tilde{H}_{kl}(\omega) = H_{kl}(\omega) + \Delta H_{kl}(\omega) + \sum_{i=m+1}^{\infty} \sum_{j=n+1}^{\infty} \Delta R(\omega), \tag{24}$$

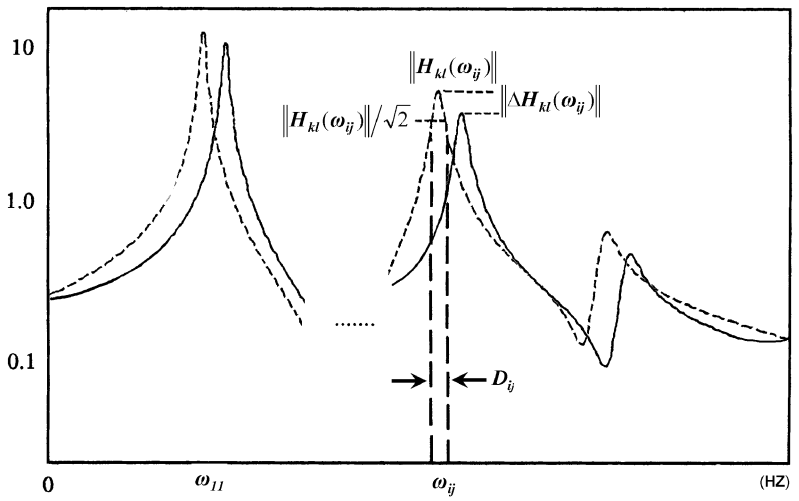


Fig. 3. $\|H_{kl}(\omega)\|$ vs. natural frequency $\omega$.

where $\Delta H_{kl}(\omega)$ and $\Delta R(\omega)$ are the residues of FRF caused by parameter variations and high order modes, respectively, and

$$\Delta H_{kl}(\omega) = \sum_{i=1}^{m} \sum_{j=1}^{n} c_{ij}(x_{s_l}, y_{s_l}) b_{ij}(x_{pe_k}, y_{pe_k}) \times \left[ \frac{1}{(\tilde{\omega}_{ij}^2 - \omega^2) + 2j\tilde{\zeta}_{ij}\tilde{\omega}_{ij}\omega} - \frac{1}{(\omega_{ij}^2 - \omega^2) + 2j\zeta_{ij}\omega_{ij}\omega} \right], \tag{25a}$$

$$\Delta R(\omega) = \frac{c_{ij}(x_{s_l}, y_{s_l}) b_{ij}(x_{pe_k}, y_{pe_k})}{(\tilde{\omega}_{ij}^2 - \omega^2) + 2j\tilde{\zeta}_{ij}\tilde{\omega}_{ij}\omega}. \tag{25b}$$

Correspondingly, the index $\beta_{ij}$ is modified as

$$\tilde{\beta}_{ij} = \frac{1}{rp} \sum_{k=1}^{r} \sum_{l=1}^{p} \left\| H_{kl}(\omega_{ij}) + \Delta H_{kl}(\omega_{ij}) + \sum_{i=m+1}^{\infty} \sum_{j=n+1}^{\infty} \Delta R(\omega_{ij}) \right\| \sqrt{\tilde{D}_{ij}}, \tag{26}$$

where $\tilde{D}_{ij} = 2\tilde{\zeta}_{ij}\tilde{\omega}_{ij} = 2(\zeta_{ij} + \Delta\zeta_{ij})(\omega_{ij} + \Delta\omega_{ij})$. It can be seen that the controllability index $\tilde{\beta}_{ij}$ deviates from its nominal value $\beta_{ij}$ due to the existence of high order modes from $\sum_{i=m+1}^{\infty} \sum_{j=n+1}^{\infty} \Delta R(\omega)$ and parameter variations from $\Delta H_{kl}(\omega_{ij})$ and $\sqrt{\tilde{D}_{ij}}$.

Detailed discussions are presented in the following sections. A flow chart showing the controllability assessment procedure is given in Fig. 4.

### 3.2.1. *Influence of unmodelled high-frequency dynamics*

The design of an effective controller is based on a good knowledge about the system dynamics, which can be readily obtained from either system identification process or structural modelling. Since active control mainly focuses on the low-frequency range, in both cases, lower order modes are usually well apprehended and used for designing the controller. Higher order modes however, can in principle, affect the control performance if they are totally ignored. The consideration of these higher order modes will render the design or the system modelling more demanding and complex. One solution is to arrange the actuator or sensor configurations in a way to minimize the contribution from these higher order modes. According to Eqs. (25b) and (26), the effect of the higher order modes on $\tilde{\beta}_{ij}$ is quantified by the term $\sum_{i=m+1}^{\infty} \sum_{j=n+1}^{\infty} \Delta R(\omega)$. It can be eliminated if either $b_{ij}$ or $c_{ij}$ in $\Delta R(s)$ is zero. $b_{ij}$ and $c_{ij}$ depend on the actuator and sensor configurations (shapes and positions), respectively. Considering that $\Delta R(s)$ is mainly contributed by the modes close to the truncated frequency, $b_{ij}$ and $c_{ij}$ can be eventually minimized through a proper design of the PZT actuators or PVDF sensors, for example, at the intersection area of the nodal lines of the corresponding strain mode shapes. It is noted that $b_{ij}$ is usually non-zero because of the size and orientation of PZTs. Although the problem can be solved theoretically by optimizing the shape and location of PZTs, it is however intractable to cut the PZT into a desired shape due to its brittle mechanical property. Based on the fact that PVDF sensor is a thin flexible film which can be easily shaped to meet the requirement, the alternative is to design PVDF configuration so that $c_{ij} = 0$. This issue is elaborated hereafter using numerical simulations.

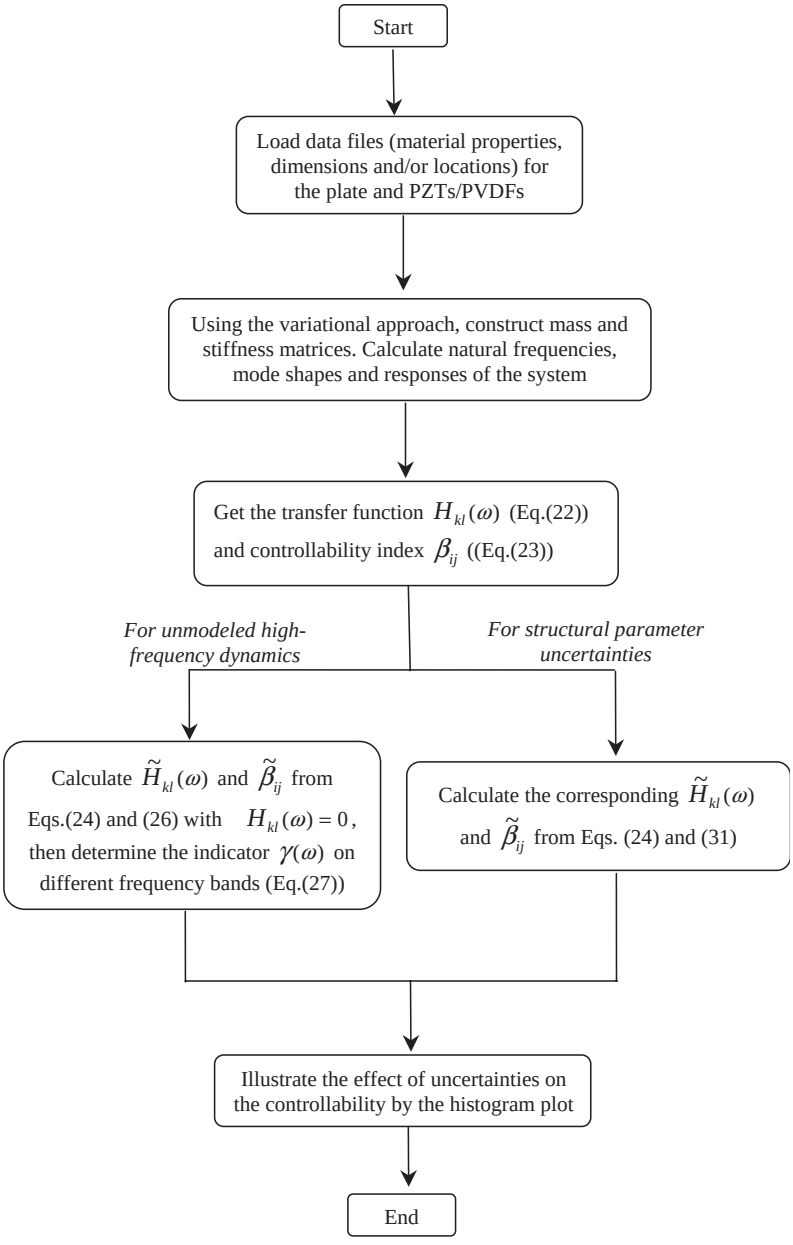


Fig. 4. Flow chart of the controllability assessment.

The structure used in numerical simulations is the same as that for experiments with a pair of PZTs and a PVDF sensor. The frequency range of interest is between 0 and 250 Hz. For simplicity, the selected modes are rearranged in the ascending order of frequencies by replacing the subscript pair $(i, j)$ of modal functions with a single $\ell$. As can be seen from Fig. 2, the number

of modes within $\omega_\ell \subset [0\ \ 250]$ Hz is 5, the PVDF sensor should thus be placed at the intersection of nodal lines of modes 6 and 7 to eliminate these two modes on $\tilde{\beta}_\ell$.

The PVDF sensor measures the overall strain of the covered area. Its design should therefore be based on strain mode shapes, which can be calculated once the displacement mode shapes are obtained. In order to explore the intersection, the distribution of nodal lines for the *first seven* strain modes with PZT actuation is analyzed and shown in Fig. 5(a). For comparison purpose, the corresponding strain mode shapes without PZTs are given in Fig. 5(b). It can be seen that the distribution of nodal lines with PZTs is highly irregular compared with their counterparts without PZTs. Apparently, the mass and stiffness added by PZTs significantly change strain mode shapes, and consequently the intersections of nodal lines. This observation suggests the consideration of the full coupling between the PZT actuators and the host plate when PVDF should be used as

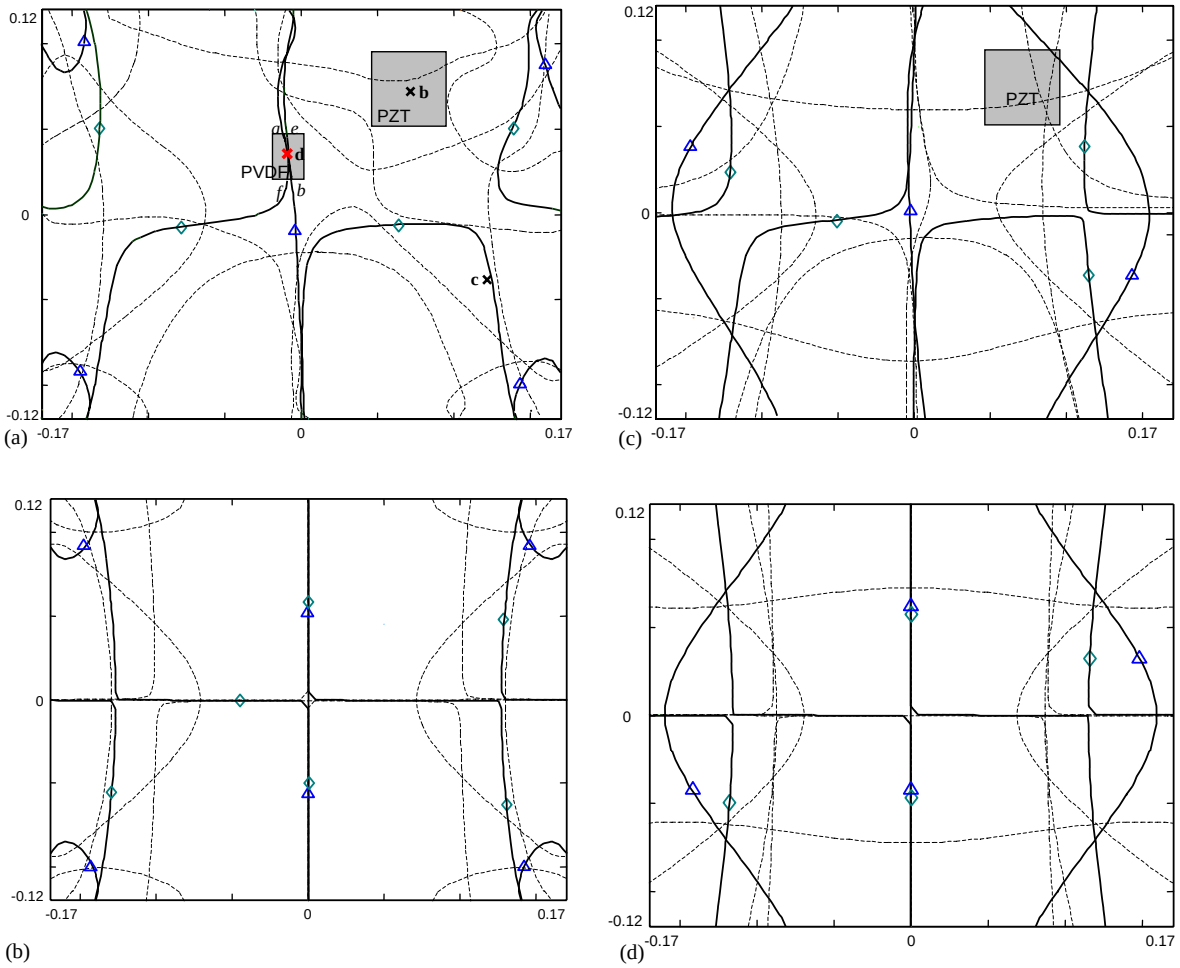


Fig. 5. Distribution of nodal lines of the first seven modes: (a) strain modes with PZT; (b) strain modes without PZT; (c) displacement modes with PZT; (d) displacement modes without PZT. Dashed: for modes 1–5; solid line: for modes 6 (‘△’) and 7 (‘◇’).

sensors. If one uses a point sensor (e.g., accelerometer), the design will be based on the displacement mode shapes only. Fig. 5(c) and (d) shows the distribution of the nodal lines for displacement mode shapes with and without PZTs, respectively. A comparison between these two figures shows a change, which is much smaller than the one observed in the case of strain mode shapes. Based on these observations, it can be concluded that PZT actuators strongly affect the strain mode shapes, but have weak effect on displacement mode shapes. When PVDF sensors are used, the dynamics of PZT actuators should be taken into account because of the high sensitivity of the strain modes.

The PZT effect on controllability index is quantitatively analyzed using different sensors. Based on the simulated FRF curves, the amplitude of $\|H(\omega_\ell)\|$, $\omega_\ell$ and $\zeta_\ell$ ($\ell = 1, \ldots, 7$) with and without PZT patches can be obtained. The corresponding controllability indices can then be calculated and normalized with their maximums. The absolute difference between indices, with and without PZT effects, is used to quantify the PZT effect. It is denoted by $|\Delta_S(\beta)|$ for the PVDF sensor and $|\Delta_D(\beta)|$ for the point sensor. Fig. 6 shows $|\Delta_S(\beta)|$ and $|\Delta_D(\beta)|$ for the first seven modes. The center of PZT is located at point **b** (0.07, 0.075). Either a PVDF sensor (with a dimension of $0.008 \times 0.012$ m$^2$) or an accelerometer is located at **c** (0.1437, −0.0387) (see Fig. 5(a)). It can be seen that due to the existence of the PZTs, the change of $|\Delta_S(\beta)|$ is significant and it reaches approximately 30% at mode 3, while the variation of $|\Delta_D(\beta)|$ is slight with a maximal of 7%. These results further confirm the conclusions drawn above.

In order to validate the effectiveness of positioning sensors in eliminating high order modes on $\tilde{\beta}_\ell$, numerical simulations are carried out using a PVDF sensor located at point **d** $(-0.0082, 0.0325)$. As can be seen in Fig. 5(a), the PVDF covers the intersection of the strain nodal lines of modes 6 and 7 (*ab* and *ef*) in a quasi-symmetrical manner. The modal responses from these two modes can therefore be expected to be very low. To further confirm this, the FRF curve of the previous case with PVDF at **c** (Fig. 7(a)) is compared to the present configuration (Fig. 7(b)). In both figures, dotted lines show the modal response of the two higher order modes

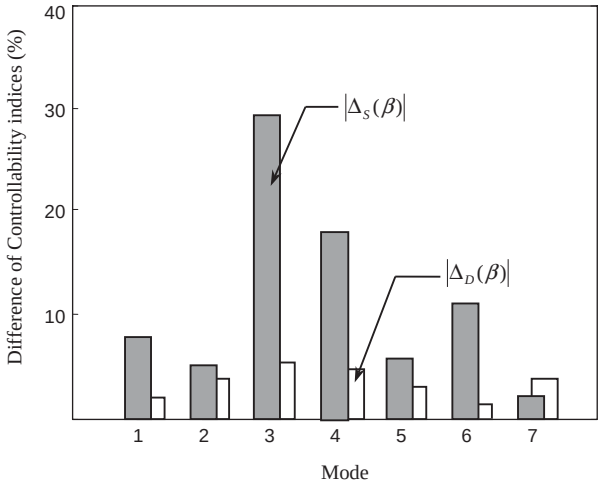


Fig. 6. The PZT effect on controllability index. Locations: PZT at (0.07, 0.075) and the sensor at (0.1437, −0.0387).

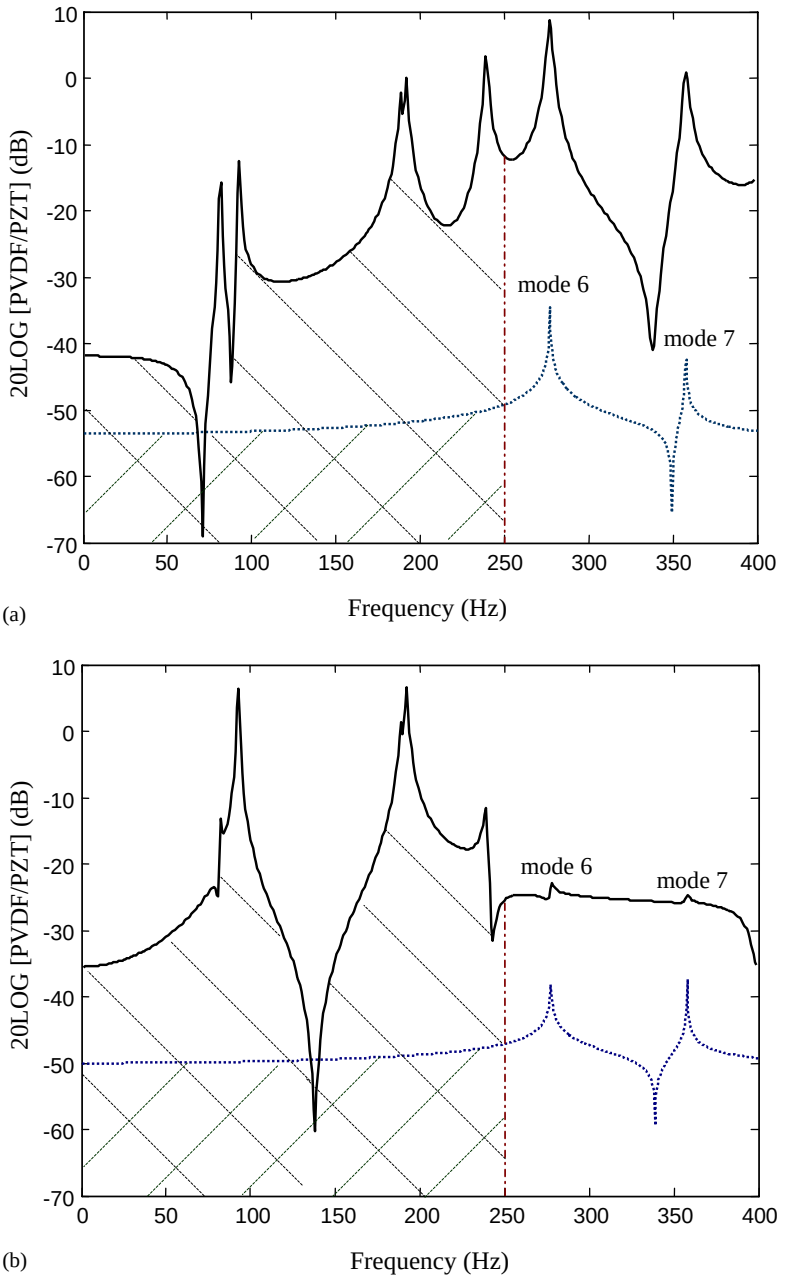


Fig. 7. The FRF with PZT at (0.07, 0.075) and PVDF at (a) (0.1437, −0.0387) and (b) (−0.0082, 0.0325). Solid line: for modes 1–7; dashed: for modes 6 and 7.

(6 and 7). It can be observed that peaks corresponding to modes 6 and 7 decrease dramatically by moving the PVDF sensor from **c** to **d**.

An indicator is defined to quantify the contribution of these two higher order modes $\sum_{\ell=6}^{7} \Delta R_\ell(\omega)$ to the total FRF $\tilde{H}(\omega)$. Since the area under the FRF curve roughly represents the

energy level within a given frequency band [22], the indicator is defined as

$$\gamma(\omega) = \frac{Area(\Delta R(\omega))}{Area(H(\omega))} \times 100\%, \tag{27}$$

where

$$Area(\Delta R(\omega)) = \int_{\omega_1}^{\omega_2} \sum_{\ell=6}^{7} \frac{c_\ell b_\ell}{(\omega_\ell^2 - \omega^2) + 2j\zeta_\ell \omega_\ell \omega} d\omega, \tag{28a}$$

$$Area(H(\omega)) = \int_{\omega_1}^{\omega_2} \sum_{\ell=1}^{7} \frac{c_\ell b_\ell}{(\omega_\ell^2 - \omega^2) + 2j\zeta_\ell \omega_\ell \omega} d\omega. \tag{28b}$$

The above definition applies to each frequency band $(\omega_2 - \omega_1)$, which is set as 50 Hz. The histogram of $\gamma(\omega)$ for the PVDF sensor locating at **c** and **d** are plotted in Fig. 8. As can be seen, the contribution of modes 6 and 7 to FRF is significantly reduced to a minimal level by the proper determination of PVDF location, e.g., the maximal one is from 4.1% for location **c** to less than 0.2% for **d** at the frequency band 0–50 Hz.

### 3.2.2. *Influence of structural parameter variations*

Once the high order modes are minimized or eventually eliminated, $\sum_{i=m+1}^{\infty} \sum_{j=n+1}^{\infty} \Delta R(\omega) = 0$. Eq. (26) is then simplified as

$$\tilde{\beta}_{ij} = \frac{1}{rp} \sum_{k=1}^{r} \sum_{l=1}^{p} \|H_{kl}(\omega_{ij}) + \Delta H_{kl}(\omega_{ij})\| \sqrt{\tilde{D}_{ij}}. \tag{29}$$

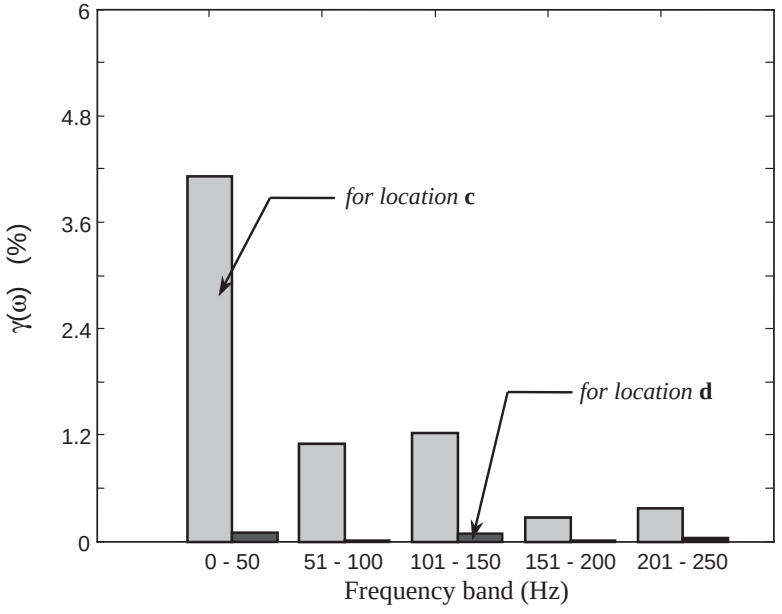


Fig. 8. Contribution of modes 6 and 7 to different frequency bands.

Denote $\tilde{D}_{ij}$ as

$$\tilde{D}_{ij} = D_{ij}(1 + \alpha_{ij}), \tag{30}$$

where $\alpha_{ij} = 2(\zeta_{ij}\Delta\omega_{ij} + \Delta\zeta_{ij}\omega_{ij} + \Delta\zeta_{ij}\Delta\omega_{ij})/D_{ij}$. Eq. (29) can be rewritten as

$$\tilde{\beta}_{ij} = \sqrt{1 + \alpha_{ij}}\left(\beta_{ij} + \frac{1}{rp}\sum_{k=1}^{r}\sum_{l=1}^{p}\|\Delta H_{kl}(\omega_{ij})\|\sqrt{D_{ij}}\right). \tag{31}$$

The above equation describes the relationship between $\tilde{\beta}_{ij}$ for the uncertain case and $\beta_{ij}$ for the nominal case. Apparently, the change of controllability index depends on the variation of parameters $(\Delta\omega_{ij}, \Delta\zeta_{ij})$ through $\alpha_{ij}$ and $\|\Delta H_{kl}(\omega_{ij})\|$. To reveal the tendency of $\tilde{\beta}_{ij}$ vs. parameter variations, cases involving slight changes in frequency, damping and boundary conditions are investigated. It is pertinent to note that these changes or uncertainties can be easily made due to an error in system identification or modelling.

For the case of frequency variation, a mass with a dimension of $(0.05 \times 0.05 \times h_m)$ is added to the structure at location $(0, -0.07)$. $h_m$ varies from 0 to 0.008 m. The introduction of additional mass will lead to a change of the natural frequencies of the plate. The histogram of the corresponding controllability index and their relative change for the first *five* modes are plotted in Fig. 9(a) and (b), respectively. It can be seen that

- For the nominal case, i.e., $h_m = 0$, $\beta_\ell$ achieves large values at modes 2 (92.65 Hz), 3 (189.16 Hz) and 4 (191.81 Hz), indicating a good controllability of these modes. This is consistent with the observation that the PZT is placed close to the largest deformation areas of these modes.
- With $h_m$ varying from 0.001 to 0.008, the overall trends of $\tilde{\beta}_\ell$ and $\beta_\ell$ are similar, e.g., $\tilde{\beta}_\ell$ reaches its maximum at mode 4 and minimum at mode 1. That is to say, this change in frequency will not fundamentally alter the characteristic of controllability of the structure.
- Fig. 9(b) shows that the relative change of controllability index is obvious and irregular, especially for those modes with close frequencies, e.g., modes 1 and 2. The reason is that with the increase of $h_m$ from 0 to 0.008, the *first two* frequencies are gradually getting closer with each other, i.e., from 81.59 and 92.65 Hz to 81.27 and 82.73 Hz, respectively. In such case, the degree of controllability for these two modes will be reconstructed, resulting in a large variation of controllability index.

For the case of damping variation, $\zeta_\ell$ $(\ell = 1, \ldots, 7)$ is increased from 0.01 (nominal case) to 0.02. The histogram of the corresponding index and the weighting of controllability degree are shown in Fig. 10(a) and (b), respectively. It can be observed that $\beta_\ell$ is not sensitive to damping variation. This is understandable in the sense that an increase in damping leads to a decrease in the peak value accompanied by an enlargement of the bandwidth. The total effect results in a relatively stable $\beta_\ell$ with respect to damping.

Slight changes in boundary conditions are considered as the last test case. As mentioned in Section 2, various boundary conditions are simulated using a set of virtual rotational ($c_i$ in N/rad, $i = 1, \ldots, 4$) or translational ($k_i$ in N/m$^2$) springs equally distributed along each edge of the plate. A proper assignment of these stiffness constants allows one to simulate cases ranging from free ($k_i = c_i = 0$) to clamped boundaries ($k_i \to \infty$, $c_i \to \infty$). In general, rigid cases can be reasonably well simulated using sufficiently high stiffness values called limit asymptotic values. In the present

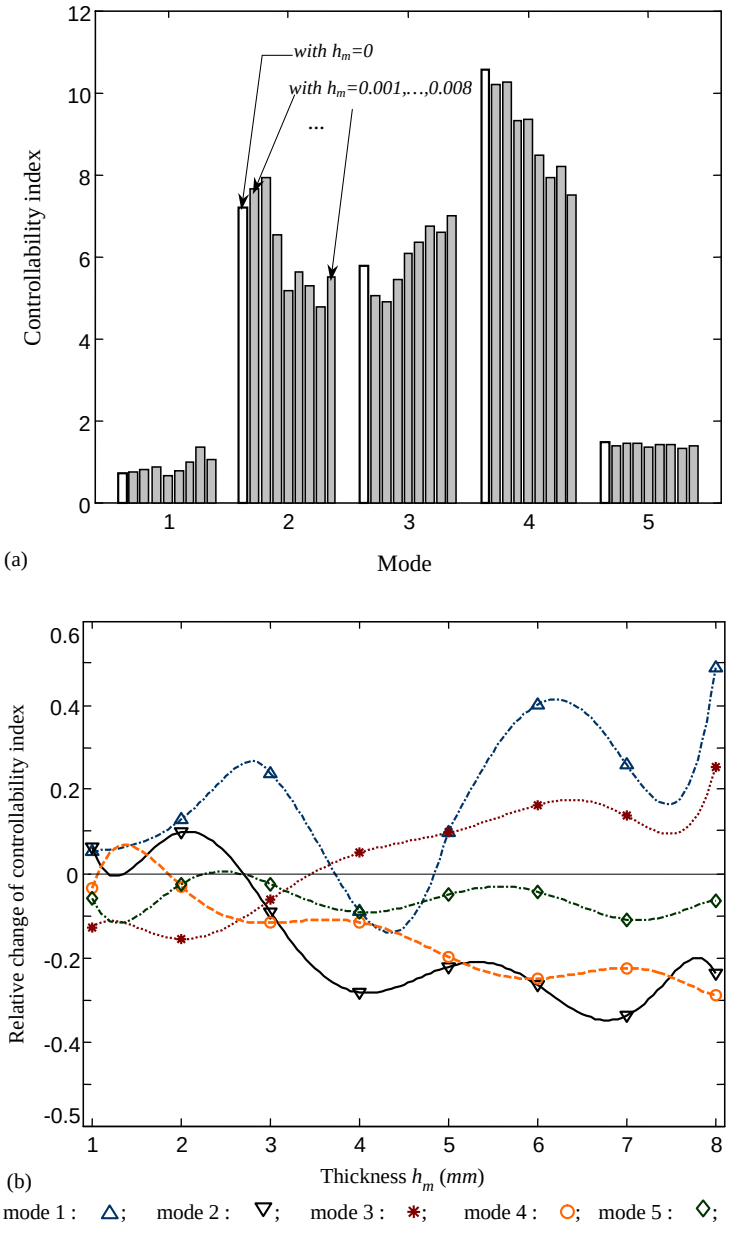


Fig. 9. (a) Controllability index with $h_m$ varying from 0 to 0.008. Location of additive mass: $(0, -0.07)$. (b) Relative change of controllability index.

case, these values are determined to be $k_c = 1 \times 10^7$ N/m$^2$ and $c_c = 1 \times 10^6$ N/rad. Since only small changes in boundaries are of concern here, a variation of 0.005–0.025% is assigned to both $k_i/k_c$ and $c_i/c_c$. Normalization to their respective limit asymptotic values would allow the comparison more meaningful and objective. In the case of translational spring, this range of

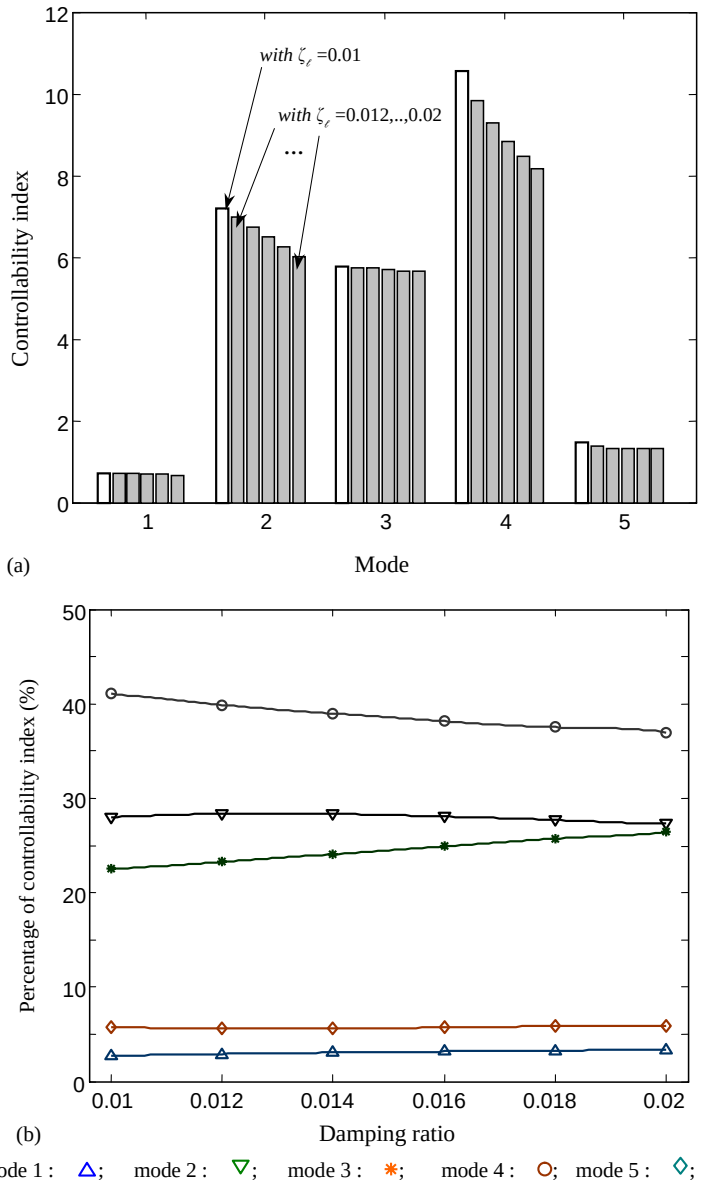


Fig. 10. (a) Controllability index with damping ratio $\zeta_\ell$ varying from 0.01 to 0.02. (b) Percentage of degree of controllability.

variation is equivalent to applying a soft support of 580–2900 N/m to a plate of 0.44 kg. The corresponding controllability indices are shown in Fig. 11(a) and (b) for different values of $k_i$ and $c_i$, respectively. It can be seen that

- With the slight increase of $k_i/k_c$, the nature of controllability keeps unchanged. For example, mode 4 is the most controllable mode among those *five*, then modes 2, 3 and so on. In addition,

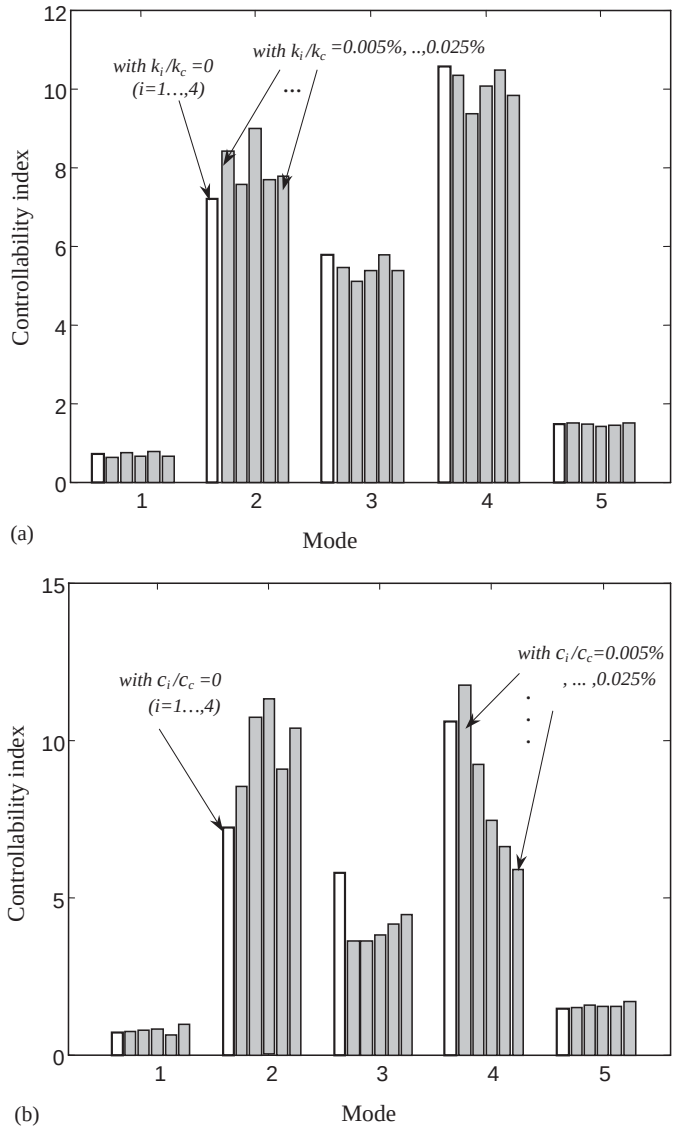


Fig. 11. (a) Controllability index with $k_i/k_c$ varying from 0.005% to 0.025%. (b) Controllability index with $c_i/c_c$ varying from 0.005% to 0.025%.

the change of degree of controllability for each mode is moderate. The maximal variation of 20% occurs at mode 2 in the case of $k_i/k_c = 0.015\%$.

- With the same increase of $c_i/c_c$, change in controllability is much more dramatic. Not only the absolute controllability of each mode but also the relative controllability between different modes is altered. A quantitative analysis of each individual mode shows a 45% reduction of controllability index for mode 4 and 40% increase for mode 2 for the case of $c_i/c_c = 0.025\%$. Apparently, even slight variations in rotational constraint can lead to

significant perturbation of the controllability of individual mode, as opposed to the case of translational one.

## 4. Conclusions

The controllability assessment of plate-like structures with uncertainties under piezoelectric actuators is performed. A novel controllability index based on the FRF rather than the controllability Gramian is proposed to quantify the degree of controllability. The state-space description of the model is developed so as to obtain the FRF between the PZTs and PVDFs, and then verified by experiments. The effects of unmodelled high-frequency dynamics and structural parameter variations on the controllability are discussed, leading to the following conclusions:

- Unmodelled higher order dynamics can be effectively minimized or eventually eliminated via a proper design of the sensor location. Since PZT actuators create significant effects on the strain mode shapes, an accurate modelling of the structure with PZTs' stiffness and mass is crucial when strain sensors are used for this purpose. These effects are, however, weak when using point transducers.
- Among all uncertainties and parameter variations considered, rotational constraint is found to be the most sensitive parameter affecting the controllability index. Special care is needed to limit its estimation error and variation in the implementation of the controllers.
- The model developed in this work can satisfactorily simulate the dynamics of plate-like structures with the consideration of the full coupling between the piezoelectric actuators and the host structure. Together with the proposed controllability index, it can further be incorporated into the whole design process, including both physical sensor/actuator arrangement and controller design.

## Acknowledgements

The authors would like to thank the Research Committee of The Hong Kong Polytechnic University and the Research Grants Council of Hong Kong Special Administrative Region for the financial support for this project (Grant No. PolyU GYY-27 and 5165/02E).

## Appendix A. Nomenclature

| | |
|---|---|
| $a \times b \times h$ | dimension of the plate (length×width×height) |
| $(\mathbf{A},\mathbf{B})$, $(\mathbf{A}_u, \mathbf{B}_u)$ | system matrices of the nominal system and the uncertain system |
| $d$ | piezoelectric strain coefficients |
| $D_0, D_k$ | equivalent flexural rigidities |
| $e_{31}, e_{32}$ | piezoelectric stress constants |
| $(E_{pl}, v_{pl})$ | Young's modulus and Poisson ratio of the plate |
| $(E_{pe}, v_{pe})$ | Young's modulus and Poisson ratio of the piezoelectric patch |
| $h_{pe}, h_{pvdf}$ | thickness of the piezoelectric patch and the PVDF |

| | |
|---|---|
| H | the Heaviside function |
| $H_{kl}(\omega), \tilde{H}_{kl}(\omega)$ | the $kl$th FRF, symbol '$\sim$' over $H$ represents the actual quantity |
| $\|\|H_{kl}(\omega_{ij})\|\|$ | Hankel singular value of $H_{kl}(\omega_{ij})$ |
| $\Delta H_{kl}(\omega)$ | the residue of FRF caused by parameter variations |
| $M_x, M_y, M_{xy}$ | resultant moments |
| $l_1, l_2$ | coefficients and $l_1 = (h + h_{pe})^3 - h^3,\ l_2 = (h + h_{pe})^2 - h^2$ |
| $(m, n)$ | numbers of the reserved modes |
| $Q(t)$ | co-ordinate transformation, $Q(t) = \dot{\eta}(t)^{\mathrm{T}}\ \eta(t)^{\mathrm{T}\mathrm{T}}$ |
| $\Delta R_{ij}(\omega)$ | the residue of FRF caused by high order modes |
| $S$ | elastic stiffness matrix |
| $V_k$ | input voltage applied on the $k$th actuator patches |
| $w$ | The mid-plane transverse displacement |
| $\mathbf{W}_c$ | controllability Gramian matrix |
| $\sigma = \sigma_x\ \sigma_y\ \sigma_{xy}{}^{\mathrm{T}}$ | stress vector |
| $\sigma_x, \sigma_y$ | normal stress |
| $\sigma_{xy}$ | shear stress |
| $\varepsilon$ | strain vector |
| $\kappa_x, \kappa_y, \kappa_{xy}$ | mid-plane mechanical curvature vector |
| $\rho$ | equivalent density of the plate ($\rho_{pl}$) and piezoelectric patch ($\rho_{pe}$) |
| $\eta_{ij}(t)$ | The $ij$th modal co-ordinate |
| $\phi_{ij}(x, y), \omega_{ij}, \zeta_{ij}$ | The $ij$th mode shape, natural frequency and damping ratio |
| $\beta_{ij}, \tilde{\beta}_{ij}$ | controllability index |
| $\gamma(\omega)$ | indicator used to quantify the contribution of high order modes |
| $\|\Delta_S(\beta)\|, \|\Delta_D(\beta)\|$ | absolute difference between indices with and without PZT effects for PVDF sensor and point sensor, respectively |
| $\Omega_{pe_k}$ | area of the $k$th piezoelectric patch |
| $\chi_{pe_k}(x, y)$ | the generalized location function |

## References


[1] W.S. Hwang, W. Hwang, H.C. Park, Vibration control of laminated composite plate with piezoelectric sensor actuator—active and passive control methods, *Mechanical Systems and Signal Processing* 8 (1994) 571–583.

[2] R. Jha, J. Rower, Experimental investigation of active vibration control using neural networks and piezoelectric actuators, *Smart Materials and Structures* 11 (2002) 115–121.

[3] Y.X. Shen, A. Homaifar, Vibration control of flexible structures with PZT sensors and actuators, *Journal of Vibration and Control* 7 (2001) 417–451.

[4] C.Q. Chen, Y.P. Shen, Optimal control of active structures with piezoelectric modal sensors and actuators, *Smart Materials and Structures* 6 (1997) 403–409.

[5] A.M. Sadri, R.J. Wynne, J.R. Wright, Robust strategies for active vibration control of plate-like structures: theory and experiment, *Proceedings of the Institution of Mechanical Engineers Part I—Journal of Systems and Control Engineering* 213 (1999) 489–504.

[6] I.Y. Shen, Stability and controllability of Euler–Bernoulli beams with intelligent constrained layer treatments, *Transactions of the American Society of Mechanical Engineers, Journal of Vibration and Acoustics* 118 (1996) 70–77.

[7] D.C. Sun, D.J. Wang, Y. Li, Z.L. Xu, Stability and controllability analysis of piezoelectric smart plates, *Progress in Natural Science* 9 (1999) 463–471.
[8] Q. Wang, C.M. Wang, Optimal placement and size of piezoelectric patches on beams from the controllability perspective, *Smart Materials and Structures* 9 (2000) 558–567.
[9] S. Leleu, H. Abou-Kandil, Y. Bonnassieux, Piezoelectric actuators and sensors location for active control of flexible structures, *IEEE Transactions on Instrumentation and Measurement* 50 (2001) 1577–1582.
[10] Q. Wang, C.M. Wang, A controllability index for optimal design of piezoelectric actuators in vibration control of beam structures, *Journal of Sound and Vibration* 242 (2001) 507–518.
[11] A.M. Hamden, A.H. Nayfeh, Measures of modal controllability and observability for first- and second-order linear systems, *American Institute of Aeronautics and Astronautics Journal of Guidance, Control, and Dynamics* 12 (1989) 421–428.
[12] A. Grace, A.J. Laub, J.N. Little, C. Thompson, *Control System Toolbox for Use with Matlab*, The MathWorks Inc., Natick, MA, 1990.
[13] C.R. Fuller, S.J. Elliott, P.A. Nelson, *Active Control of Vibration*, Academic Press, London, 1996.
[14] B.T. Wang, C.A. Rogers, Laminate Plate theory for spatially distributed induced strain actuators, *Journal of Composite Materials* 25 (1991) 433–452.
[15] H.T. Banks, R.C. Smith, Y. Wang, The modeling of piezoelectric patch interactions with shells, plates and beams, *Quarterly of Applied Mathematics* 53 (1995) 353–381.
[16] B. Proulx, L. Cheng, Dynamic analysis of piezoceramic actuation effects on plate vibrations, *Thin-Walled Structures* 37 (2000) 147–162.
[17] Y. St-Amant, L. Cheng, Simulations and experiments on active vibration control of a plate with integrated piezoceramics, *Thin-Walled Structures* 38 (2000) 105–123.
[18] Y.Y. Li, L. Cheng, L.H. Yam, Y.J. Yan, Numerical modeling of a damaged plate with piezoelectric actuation, *Smart Materials and Structures* 12 (2003) 524–532.
[19] W. Chang, S.V. Gopinathan, V.V. Varadan, V.K. Varadan, Design of robust vibration controller for a smart panel using finite element model, *Journal of Vibration and Acoustics* 124 (2002) 265–275.
[20] W. Gawronski, J.N. Juang, Model reduction for flexible structures, *Control and Dynamic Systems* 36 (1990) 143–222.
[21] Y.Y. Li, L.H. Yam, Study on model order determination of thin plate systems with parameter uncertainties, *Mechanical Systems and Signal Processing* 13 (1999) 667–680.
[22] L. Cheng, R. Lapointe, Vibration attenuation of panel structures by optimally shaped viscoelastic coating with added weight considerations, *Thin-Walled Structures* 21 (1995) 307–326.